

# Machine learning empowered thin film acoustic wave sensing

Cite as: Appl. Phys. Lett. **122**, 014101 (2023); doi: 10.1063/5.0131779

Submitted: 24 October 2022 · Accepted: 23 December 2022 ·

Published Online: 4 January 2023



View Online



Export Citation



CrossMark

Kaitao Tan,<sup>1</sup> Zhangbin Ji,<sup>1</sup> Jian Zhou,<sup>1,a)</sup> Zijing Deng,<sup>1</sup> Songsong Zhang,<sup>2</sup> Yuandong Gu,<sup>2</sup> Yihao Guo,<sup>1</sup> Fengling Zhuo,<sup>1</sup> Huigao Duan,<sup>1</sup> and YongQing Fu<sup>3</sup>

## AFFILIATIONS

<sup>1</sup>College of Mechanical and Vehicle Engineering, Hunan University, Changsha 410082, China

<sup>2</sup>Shanghai Industrial μTechnology Research Institute (SITRI), 235 Chengbei Rd., 201800 Shanghai, China

<sup>3</sup>Faculty of Engineering and Environment, Northumbria University, Newcastle upon Tyne NE1 8ST, United Kingdom

<sup>a)</sup>Author to whom correspondence should be addressed: [jianzhou@hnu.edu.cn](mailto:jianzhou@hnu.edu.cn)

## ABSTRACT

Thin film-based surface acoustic wave (SAW) technology has been extensively explored for physical, chemical, and biological sensors. However, these sensors often show inferior performance for a specific sensing in complex environments, as they are affected by multiple influencing parameters and their coupling interferences. To solve these critical issues, we propose a methodology to extract critical information from the scattering parameter and combine the machine learning method to achieve multi-parameter decoupling. We used the AlScN film-based SAW device as an example in which the highly c-axis orientated and low stress AlScN film was deposited on silicon substrate. The AlScN/Si SAW device showed a Bode quality factor value of 228 and an electromechanical coupling coefficient of ~2.3%. Two sensing parameters (i.e., **ultraviolet or UV** and temperature) were chosen for demonstration, and the proposed machine learning method was used to distinguish their influences. Highly precision UV sensing and temperature sensing were independently achieved without their mutual interferences. This work provides an effective solution for decoupling of multi-parameter influences and achieving anti-interference effects in thin film-based SAW sensing.

Published under an exclusive license by AIP Publishing. <https://doi.org/10.1063/5.0131779>

Surface acoustic wave (SAW) devices have been widely used for sensors, such as mass,<sup>1,2</sup> temperature,<sup>3,4</sup> humidity,<sup>5–7</sup> UV,<sup>8–10</sup> gas molecules,<sup>11,12</sup> and biomolecules.<sup>12,13</sup> Conventional SAW devices are fabricated on bulk piezoelectric materials (such as LiNbO<sub>3</sub> and quartz) because of their low cost, smooth surface, stable material parameters, and high acoustic-electric conversion efficiency.<sup>2,11</sup> However, these conventional bulk piezoelectric materials have issues such as limited SAW propagation velocities and/or poor capabilities to be integrated into processes for silicon-based integrated circuits (ICs). To overcome these limitations, thin film acoustic wave devices based on piezoelectric thin film materials, such as zinc oxide (ZnO) and aluminum nitride (AlN), have been developed, as these piezoelectric films can be deposited onto non-piezoelectric substrates such as silicon with the advantage of IC process compatibility. Compared to ZnO films, AlN films show a much higher SAW velocity,<sup>14</sup> which is suitable for high frequency (thus high sensitivity) sensing, and have advantages of better mechanical properties,<sup>15</sup> better chemical stability in acid/alkali, and higher operating temperatures.<sup>9,16</sup> However, AlN films have low electromechanical coupling coefficients ( $K^2$ ), such as ~0.5%, which is

much lower than those of other piezoelectric materials (LiNbO<sub>3</sub>, 7%) or thin films (ZnO, 2%).<sup>17</sup> This severely limits its application in sensors. To solve this engineering challenge, researchers have developed the AlScN film in which an appropriate concentration of scandium (Sc) doped in AlN films can significantly improve the piezoelectric properties of AlN. For example,  $K^2$  value of AlScN based SAW devices can be increased up to 4%,<sup>18</sup> which is suitable for high performance sensors and integrated lab-on-chips.<sup>19</sup>

Although there are rapid developments with thin film-based SAW technology, severe challenges are still remained for their applications. For example, one of the key challenges to develop highly sensitive SAW sensors is that it is simultaneously sensitive to multiple parameters or factors (e.g., temperature, UV, humidity, vibration, or electromagnetic noise, etc.), apart from the real and targeted parameters. One commonly applied solution is to use a differential circuit to eliminate the interferences of other parameters,<sup>15</sup> however, this often leads to complicated signal processing circuit and test equipment. Another commonly used method is to find the differences based on different wave modes of the same SAW device.<sup>20,21</sup> However, this

method has some limitations; for example, it cannot be applied to various types of SAW devices. Therefore, great challenges are still remained to decouple multi-sensitive parameters of thin film-based SAW sensors.

In this study, we proposed to extract multiple features from scattering parameters of SAW device and then use machine learning methods [i.e., using support vector machine (SVM)<sup>22,23</sup> and random forest regression (RFR)<sup>24–26</sup>] for training models to distinguish multiple sensitive signals and achieve multi-parameter decoupling. In this study, we will take the AlScN film SAW device as an example. The highly c-axis orientated and low stressed AlScN (with Sc concentration of ~9%) film was deposited on silicon, and AlScN film-based SAW devices were fabricated [Figs. 1(a) and 1(b)]. Its Bode Q value is up to 228, and its  $K^2$  value is ~2.3%. We selected two sensitive parameters of UV and temperature as demonstration examples [Figs. 1(a) and 1(b)]. The information extracted from the SAW's transmission parameters (e.g.,  $S_{21}$ ) was used as features, sensitive parameters (e.g., ambient temperature and UV intensity) were set as labels into the model for training, and then the relationship between the features and the labels using the machine learning methods was fit to obtain a trained model, which predicted the corresponding sensitive parameters [see Fig. 1(c)]. Both high-precision UV sensing and temperature sensing were independently achieved without the interferences by each other for these AlScN film-based SAW devices.

AlScN films were deposited on silicon using a magnetron sputtering system. Crystal orientation, surface morphology, cross-sectional morphology, element composition, and molecular structure of the AlScN film were characterized, and detailed procedures were shown in

the supplementary material. Standard UV photolithography and lift-off processes were used to fabricate two-port SAW resonators on the AlScN/Si layered structure with different wavelengths ( $\lambda$ ) of 16, 20, and 24  $\mu\text{m}$ , with their detailed information shown in supplementary material. The transmission ( $S_{21}$ ) and reflection ( $S_{11}$ ) spectra of the SAW devices were obtained using a vector network analyzer (Ceyear 3656D, China). We selected two SAW sensitive parameters as demonstrators, i.e., UV and temperature. The UV and temperature testing procedures are shown in the supplementary material. We conducted 16 groups of UV response experiments at 16 different temperature points (from 30 to 50 °C), as listed in Table S1.

Figure 2(a) shows a single and sharp peak at two theta angle of 35.9° in the x-ray diffractometer (XRD) spectrum, indicating that the deposited AlScN film has a preferred (0002) crystal orientation. The full width at half-maximum of the (0002) crystal orientation for the XRD curve is 0.0498°, corresponding to an estimated mean grain size of about 43.39 nm based on Scherrer's equation.<sup>5</sup> The axial stress was estimated to be ~25.53 MPa, showing that the deposited film has a low residual stress on the Si substrate. Inset in Fig. 2(a) shows surface morphology and roughness of the film, and the root-mean square roughness (RMS) was measured to be ~1.17 nm over an area of  $10 \times 10 \mu\text{m}^2$ , which is much smoother than that reported in a previous study.<sup>27</sup> Figure 2(b) shows a scanning electron microscope (SEM) image of the AlScN film, revealing the columnar structures of AlScN nanocrystals, perpendicular to the substrate with an average thickness of ~2  $\mu\text{m}$ . Results show that a high-quality AlScN piezoelectric film with c-axis preferred orientation, low stress, and low surface roughness has been deposited on the Si substrate.

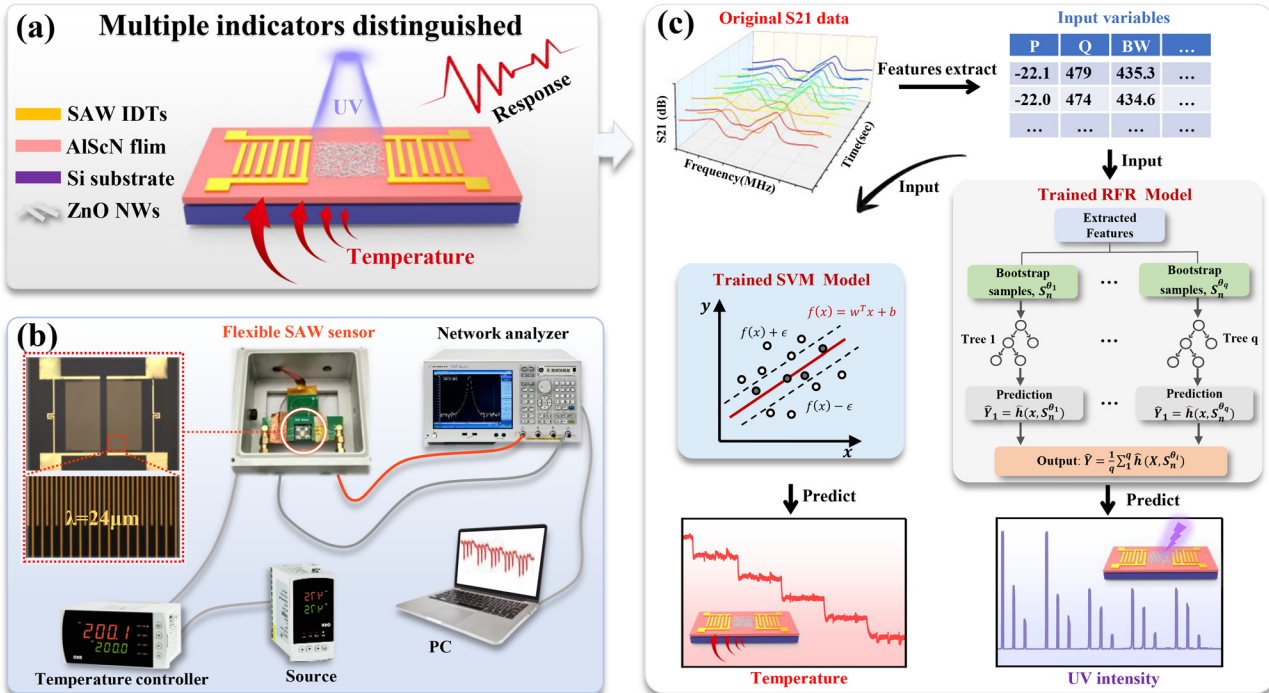


**FIG. 1.** (a) Schematic structure of AlScN film-based SAW devices and schematic sensing diagram of temperature and UV sensing; (b) schematic view of the testing system used for temperature and UV sensing of AlScN film-based SAW; (c) model of machine learning for AlScN film-based SAW sensors.

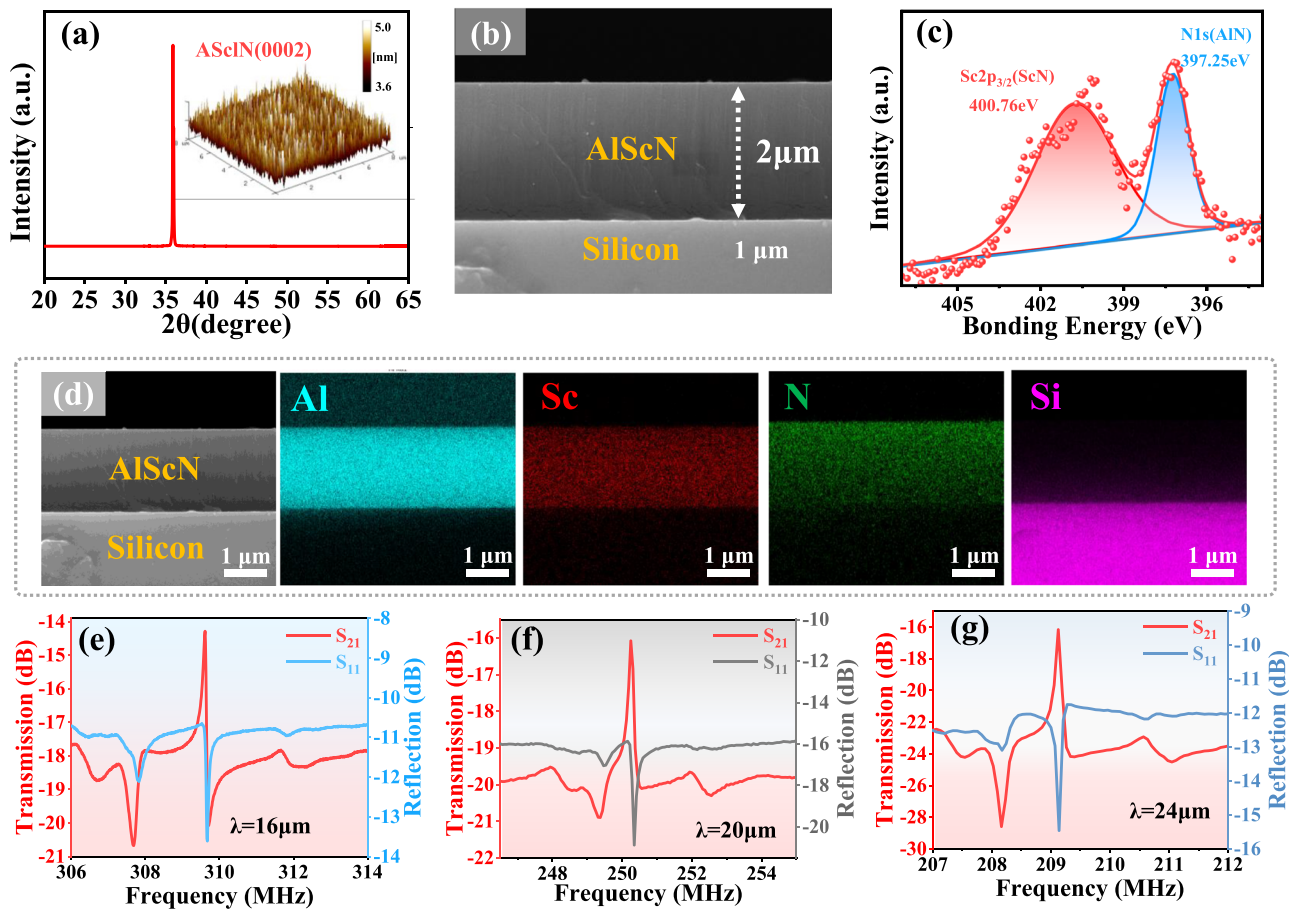


**FIG. 2.** Characterization of the AlScN thin film deposited on the silicon wafer substrate: (a) XRD pattern of the AlScN film, showing strong (0002) orientation, and AFM image of the AlScN film, showing the smooth surface; (b) SEM image of the cross section of the AlScN film; (c) XPS high-resolution spectra of Al 2p and N 1s of the AlScN films. (d) The element distribution in the AlScN/Si layered structure obtained using an EDS; (e)–(g) the transmission and reflection spectra of AlScN/Si SAW devices.

From the x-ray photoelectron microscope (XPS) analysis, two binding energy components of N 1s were obtained after peak deconvolution using a curve-fitting program, and those at binding energies of 397.25 and 400.20 eV are corresponding to Al-N and Sc-N bonds, as shown in Fig. 2(c). Energy dispersive spectroscopy (EDS) in Fig. 2(d) indicates that the Al, Sc, and N elements in the AlScN thin films have uniform distributions, and the obtained percentages of N, Al, and Sc elements are 35.91 wt.%, 55.25 wt.%, and 8.84 wt.% corresponding to 53.33 at.%, 42.59 at.%, and 4.09 at.%, respectively.

Figures 2(e)–2(g) show electrical performance of AlScN/Si SAW devices, showing clear generations of Rayleigh resonance peaks with resonant frequencies of 309.61, 250.25, and 209.16 MHz for the  $\lambda$  of 16, 20, and 24  $\mu\text{m}$ . We have fabricated four batches of SAW devices, and their resonant frequencies with the same wavelength are very close (with relative deviation less than 0.05%). The phase velocities ( $v_p$ ) of these SAW devices,  $v_p = \lambda f_0$ , were calculated to be 4953.76, 5005.00, and 5019.84  $\text{m s}^{-1}$ , which are increased gradually with an increase in wavelength from 16 to 24  $\mu\text{m}$ . High performance SAW devices and high-precision SAW sensors should have both the high  $Q$  value and  $K^2$ . We have obtained the  $Q$  value of 228 and  $K^2$  of 2.3% for the device

with a  $\lambda$  of 24  $\mu\text{m}$ , showing much better performance than that of the AlScN/Si SAW device reported in Ref. 28.

Figures 3(a) and S1 show the changes of resonant frequency, phase angle, and insertion loss of the SAW device ( $\lambda$  of 24  $\mu\text{m}$ ) under different UV intensities and various temperatures (testing conditions are listed in Table S1). When the testing temperature is 30.4 °C, the frequency shifts of the resonance increase with the increase in UV light intensity, as shown in Fig. 3(a). In addition, the phase angles and insertion loss of the resonant mode are observed to increase simultaneously with the increase in UV intensity, as shown in Fig. 3(a). As it is well-known, UV responses of SAW devices are mainly based on acoustoelectric effects. The generated free carriers (electron-hole pairs) induced by the UV irradiations interact with the acoustic waves field, resulting in the changes of transmission characteristics including acoustic wave velocity, attenuation of wave amplitude, and phase angle. These changes of the SAW properties can be written using the following equation:<sup>29</sup>

$$\frac{\Delta\nu}{\nu} = \frac{\nu - \nu_{sc}}{\nu_{oc}} - \frac{k^2}{2} \frac{1}{1 + (\sigma_d/\sigma_M)^2}, \quad (1)$$

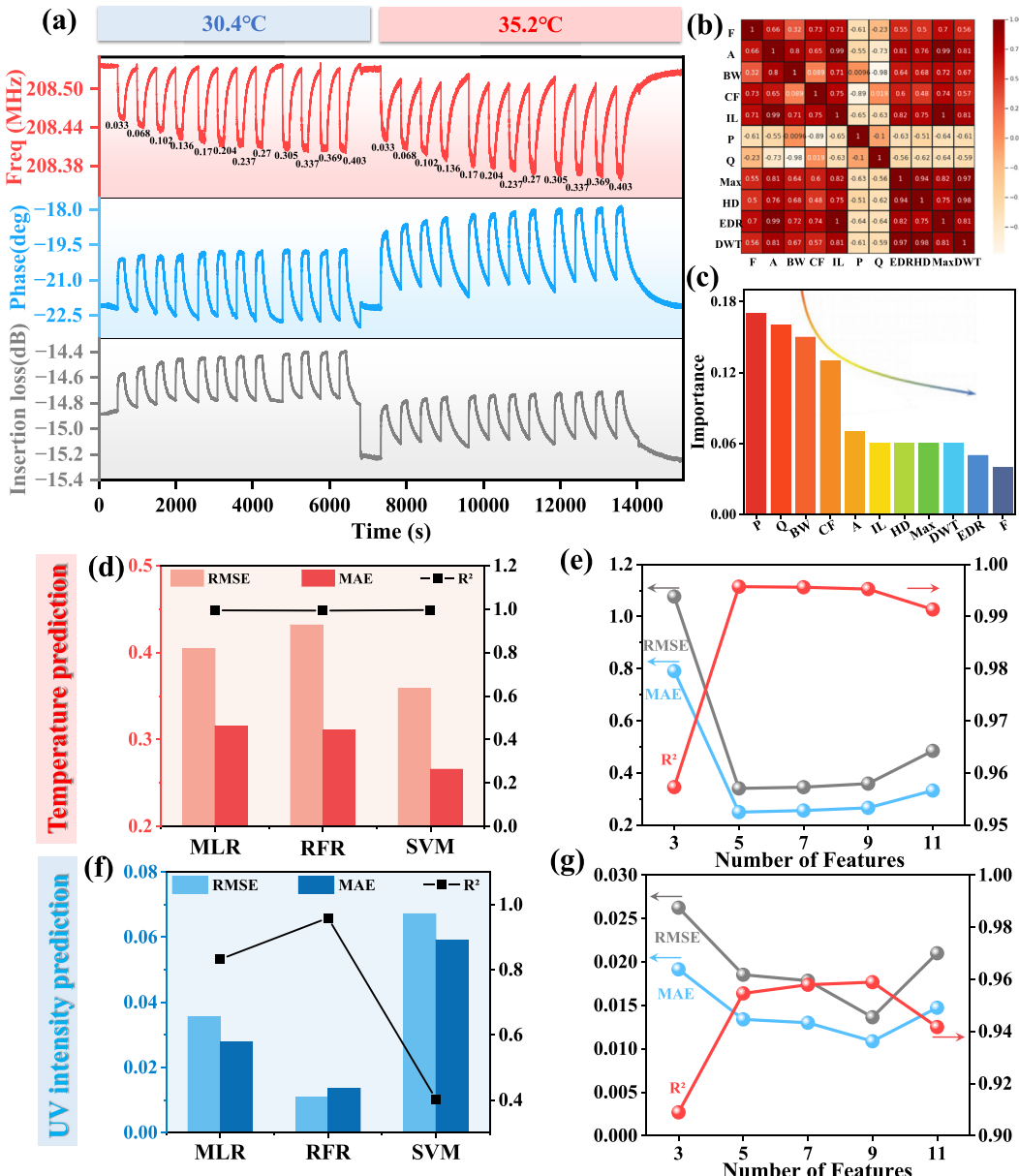


**FIG. 3.** (a) Frequency, insertion loss, and phase responses of SAW devices under different UV light intensity and temperatures; (b) different features correlation coefficient matrix; (c) importance of each feature; (d) the performance of three algorithms (MLR, RFR, and SVM) on temperature prediction; (e) the metrics of MAE, root-mean-square-error (RMSE), and  $R^2$  for temperature prediction results using different number of features (3, 5, 7, 9, and 11); (f) the performance of three algorithms (MLR, RFR, and SVM) on UV intensity prediction; (g) the metrics of MAE, RMSE, and  $R^2$  for UV light intensity prediction results using different number of features (3, 5, 7, 9, and 11).

$$\Gamma = \frac{k^2 \pi}{2} \frac{\sigma / \sigma_M}{\lambda} \frac{1}{1 + (\sigma / \sigma_M)^2}, \quad (2)$$

$$\Delta\varphi = 2\pi \frac{L \Delta v}{\lambda v}, \quad (3)$$

where  $v_{oc}$  is the SAW velocity on a free surface,  $\Delta v$  is the velocity shift,  $k^2$  is the effective electromechanical coupling coefficient,  $\sigma$  is the sheet

conductivity,  $\sigma_M$  is a material constant,  $\Gamma$  is the attenuation,  $\lambda$  is the SAW wavelength,  $\Delta\varphi$  is the phase angle, and  $L$  is the acoustic path length.

When the SAW device is at a higher temperature (e.g., 35.2 °C), UV responses of the SAW device show similar trends. However, the change of temperature (e.g., from 30.4 to 35.2 °C) will also change the resonant frequency, phase, insertion loss, and other characteristics of SAW devices [Fig. 3(a)]. These results demonstrated that both the UV

and temperature will affect the characteristics of SAW devices and would interfere with each other.

We selected two sensitive parameters, i.e., UV and temperature, as examples and apply machine learning algorithms to distinguish these two sensitive parameters. In order to improve the accuracy of machine learning algorithms, we need to maximize the extracted useful information from the original data as features and then use these features as the inputs of machine learning algorithms. The frequency responses within the frequency band (205–210 MHz, near the resonant frequency) of  $S_{21}$  spectra were chosen as the original data. Frequency-amplitude responses of  $S_{21}$  in this band were composed of 201 points and regarded as a 201-dimensional vector. Each original vector was assumed to reduce dimension by a nonlinear mapping to obtain 11 features, including Frequency (F), Amplitude (A), Band width (BW), Center frequency (CF), Insertion Loss (IL), Phase (P), Q value (Q), Hausdorff distance (HD), Edit distance on real sequence (EDR), Maximum value (MAX), and Dynamic time warping (DTW). These features include the intrinsic physical variation characteristics of the SAW responses (e.g., F, A, BW, CF, IL, P, and Q) and the variation characteristics for the  $S_{21}$  curves of the SAW device (e.g., HD, EDR, DTW, and MAX).<sup>30–32</sup> Reducing dimension using a nonlinear mapping is beneficial for simplifying calculations and preventing the overfitting. The calculation methods for these 11 features are shown in the supplementary material for more details. These eleven features are changed with the changes of UV intensity from 0.033 to 0.403 mw/cm<sup>2</sup>, at the temperature of 31.7 °C as shown in Fig. S2.

We used three metrics, including mean absolute error (MAE), root-mean square error (RMSE), and  $R^2$  values to evaluate the performance of the model.<sup>33</sup> The MAE is defined as follows:

$$MAE = \frac{1}{n} \sum_{i=1}^n |y_i - \hat{y}_i|, \quad (4)$$

where  $n$  represents the number of observations,  $y_i$  represents the experimental values, and  $\hat{y}_i$  represents the predicted values. This metric calculates the mean of the absolute sum of the errors of the predicted and true values and is used to evaluate how close the predicted results are to the real data. A smaller MAE value indicates a higher accuracy of the prediction results, whereas RMSE is frequently used to measure the differences between values predicted by the model and the observed experimental values. The RMSE should be as small as possible, which is defined as

$$RMSE = \sqrt{\frac{\sum_{i=1}^n (y_i - \hat{y}_i)^2}{n}}, \quad (5)$$

where  $R^2$  is another indicator that indicates how closely the predicted values from a model matched with the observed values and is defined as

$$R^2 = 1 - \frac{\sum_{i=1}^n (y_i - \hat{y}_i)^2}{\sum_{i=1}^n (y_i - \bar{y})^2}. \quad (6)$$

The ideal  $R^2$  value for a model should be 1. The closer it is to 1, the stronger the model's ability to interpret the predicted value, and the better the model fits the data.

We have compared the performance of three different machine learning regression algorithms, i.e., multiple linear regression

(MLR), support vector machine (SVM), and random forest regression (RFR), for the temperature and UV light intensity predictions [Figs. 3(d) and 3(f)]. Results show that the SVM model shows the best performance for temperature prediction, which generates the smallest prediction error (using the MAE and RMSE) and the largest  $R^2$ . The RFR model has the best performance in UV light intensity prediction. Accordingly, we chose to use the SVM model to predict temperature and use the RFR model to predict UV light intensity. The feature data of the training set were put into these two models with temperature labels and UV intensity labels, respectively, for training processes. The testing sets were then used to evaluate the model's performance. By comparing the actual temperatures and UV light intensities from the experiments with the predicted ones, the prediction accuracy of the model was evaluated.

It is well-known that different features do not contribute equally to model, and some features may be highly correlated with each other, which can result in redundant features.<sup>34</sup> Too many or invalid features will lead to performance degradation of the proposed model. The correlation coefficient matrix [Fig. 3(b)], together with the estimated importance of each feature obtained using a random forest algorithm,<sup>33</sup> was used to determine the priority of features [Fig. 3(c)]. The top 3, 5, 7, 9, and 11 features with the highest importance were selected to construct the model, and their performance on temperature and UV intensity predictions was compared. The results are shown in Figs. 3(e) and 3(g). When the number of input features is 5, the model has the best temperature prediction effect with the smallest error (MAE = 0.25, RMSE = 0.34), and also the largest  $R^2$  of 0.996. For UV light intensity predictions, the optimal number of input features is 9 (with values of MAE = 0.011, RMSE = 0.0136, and  $R^2$  = 0.959). Therefore, in the follow-up studies, the SVM model with five features was used to predict temperature, and the RFR model with nine features was used for UV light intensity prediction. Both these two models include five features, i.e., phase, Q value, band width, center frequency, and amplitude. Compared with those temperature predictions, UV intensity predictions require extra four features (e.g., Hausdorff distance, maximum value, dynamic time warping, and insertion loss).

After optimizing the model algorithm, we further did UV test using the fabricated SAW devices to verify the proposed model, by varying temperatures from 50 °C to 31 °C. Figure 4(a) shows the obtained resonant frequency responses of the SAW device under dynamically changed temperatures and ultraviolet environments.

In order to show the temperature prediction results of the model, we used the traditional linear regression and our model after training based on SVM to predict the temperature value of the test data, and their results were then compared with the actual values. The obtained results are shown in Fig. 4(b), which indicates that due to the interference of ultraviolet environment, the traditional linear regression (i.e., using a linear function fitting based on the relationship between frequency and temperature) has a larger deviation in temperature prediction. Whereas our proposed training model has shown a better prediction effect, proving the validity of our proposed SVM in SAW temperature prediction.

Similarly, the prediction results of UV intensity are shown in Fig. 4(c). When using the traditionally linear regression for UV analysis, the analysis results are deviated significantly from the actual UV intensity data. This is because the frequency changes caused by the

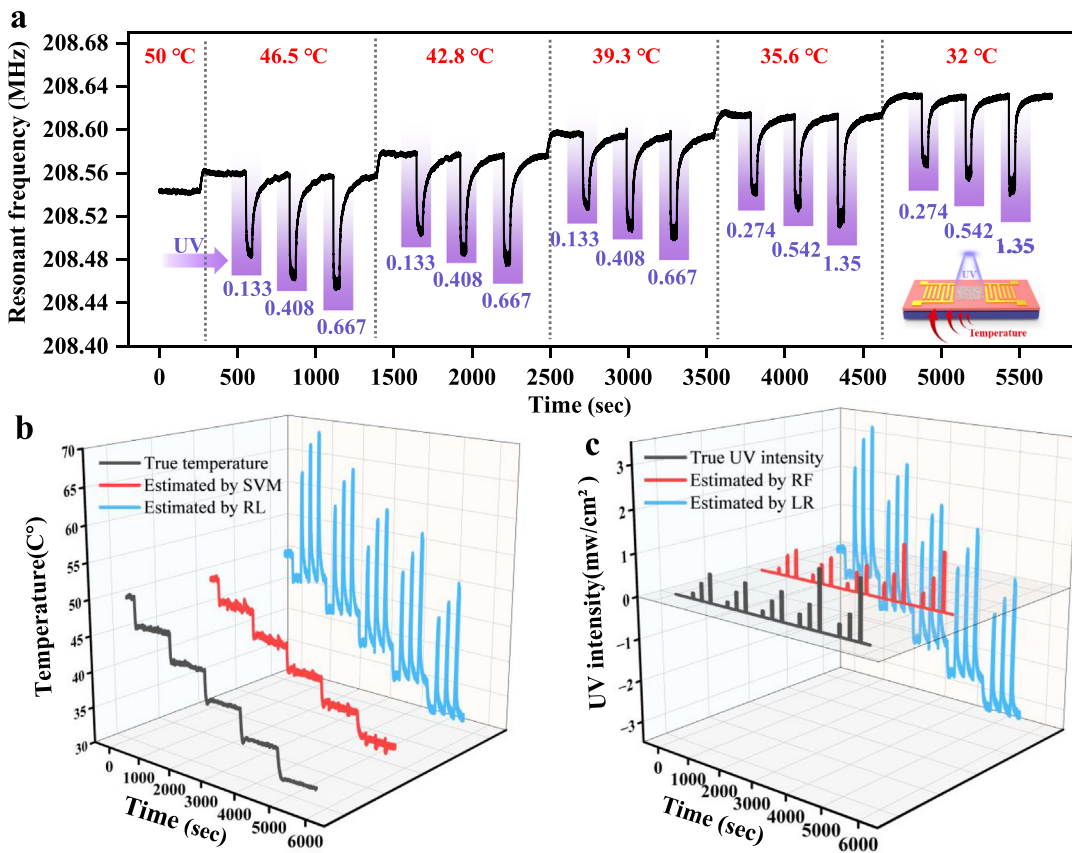


**FIG. 4.** (a) Resonant frequency of SAW devices under different UV light intensity and temperatures (test experiment). (b) Comparison of the temperature predicted results by the traditional linear regression and the SVM model. (c) Comparison of the UV intensity predicted results by the traditional linear regression and the RFR model.

temperature changes were also treated as the influences of UV changes. However, when the results of SAW devices were compared to those obtained from our proposed machine learning method (RFR), the predicted results agreed well with the actual UV intensities.

We further did multiple UV sensing tests with temperatures varied from 32 to 38 °C for the SAW devices with wavelengths of 20 and 16 μm, and the obtained results are shown in Figs. S3 and S4. Results demonstrate that the proposed machine learning algorithm effectively achieve decoupling of multiple parameters, and our model is applicable to the different SAW devices with different wavelengths. All these results clearly demonstrate the potentials using the proposed machine learning method to enable the SAW device realizing accurate measurement of multiple physical quantities at the same time.

In brief, highly c-axis orientation and low-stressed AlScN film was deposited on the silicon substrate in this study. The AlScN film-based SAW devices showed a Q value up to 228, and  $K^2$  of 2.3%. We then proposed a strategy by extracting more information from the scattering parameter and combined the machine learning method (e.g., SVM and RFR) to train a model to achieve multi-parameter decoupling for the AlScN film-based SAW device. As proof-of-concept demonstrations, we took UV and temperature sensing as examples,

and we have demonstrated the effective decoupling of these two parameters, simultaneously and accurately. This work provides an effective solution for multi-parameter decoupling of the film-based SAW sensor and realizing high-precision anti-interference sensing.

See the [supplementary material](#) for the detailed calculation methods about 11 features of SAW and all experimental data used for model training and model prediction results of SAW devices based on different wavelengths.

This work was supported by the NSFC (No. 52075162), the Program of New and High-tech Industry of Hunan Province (Nos. 2020GK2015 and 2021GK4014), the Excellent Youth Fund of Hunan Province (No. 2021JJ20018), the Key Research & Development Program of Guangdong Province (No. 2020B0101040002), and the International Exchange Grant (No. IEC/NSFC/201078) through Royal Society UK and the NSFC.

## AUTHOR DECLARATIONS

### Conflict of Interest

The authors have no conflicts to disclose.

**Author Contributions**

Kaitao Tan and Zhangbin Ji contributed equally to this work.

**Kaitao Tan:** Conceptualization (equal); Data curation (equal); Investigation (equal); Methodology (equal); Writing – original draft (equal). **Yongqing Fu:** Validation (equal); Writing – original draft (equal); Writing – review & editing (lead). **Zhangbin Ji:** Conceptualization (equal); Data curation (equal); Formal analysis (equal); Methodology (equal); Writing – original draft (equal). **Jian Zhou:** Conceptualization (equal); Funding acquisition (equal); Supervision (equal); Writing – original draft (equal); Writing – review & editing (equal). **Zijing Deng:** Resources (equal); Writing – review & editing (equal). **Songsong Zhang:** Formal analysis (equal); Project administration (equal); Writing – original draft (equal). **Yuandong (Alex) Gu:** Methodology (equal); Writing – original draft (equal). **Yihao Guo:** Data curation (equal); Validation (equal); Visualization (equal). **Fengling Zhuo:** Validation (equal); Visualization (equal); Writing – original draft (equal). **Huigao Duan:** Funding acquisition (equal); Resources (equal); Writing – review & editing (lead).

**DATA AVAILABILITY**

The data that support the findings of this study are available from the corresponding authors upon reasonable request.

**REFERENCES**

- <sup>1</sup>J. Zheng, J. Zhou, P. Zeng, Y. Liu, Y. Shen, W. Yao, Z. Chen, J. Wu, S. Xiong, Y. Chen, X. Shi, J. Liu, Y. Fu, and H. Duan, *Appl. Phys. Lett.* **116**(12), 123502 (2020).
- <sup>2</sup>Z. Chen, J. Zhou, H. Tang, Y. Liu, Y. Shen, X. Yin, J. Zheng, H. Zhang, J. Wu, X. Shi, Y. Chen, Y. Fu, and H. Duan, *ACS Sens.* **5**(6), 1657 (2020).
- <sup>3</sup>J. Zhou, D. Zhang, Y. Liu, F. Zhuo, L. Qian, H. Li, Y.-Q. Fu, and H. Duan, “Record-breaking frequency of 44 GHz based on the higher order mode of surface acoustic waves with  $\text{LiNbO}_3/\text{SiO}_2/\text{SiC}$  heterostructures,” *Engineering* (in press 2022).
- <sup>4</sup>L. Lamanna, F. Rizzi, F. Guido, L. Algieri, S. Marras, V. M. Mastronardi, A. Qualtieri, and M. De Vittorio, “Flexible and transparent aluminum-nitride-based surface-acoustic-wave device on polymeric polyethylene naphthalate,” *Adv. Electron. Mater.* **5**(6), 1900095 (2019).
- <sup>5</sup>J. Wu, C. Yin, J. Zhou, H. Li, Y. Liu, Y. Shen, S. Garner, Y. Fu, and H. Duan, “Ultrathin glass-based flexible, transparent, and ultrasensitive surface acoustic wave humidity sensor with  $\text{ZnO}$  nanowires and graphene quantum dots,” *ACS Appl. Mater. Interfaces* **12**(35), 39817 (2020).
- <sup>6</sup>J. Zhou, Z. Ji, Y. Guo, Y. Liu, F. Zhuo, Y. Zheng, Y. Gu, Y. Fu, and H. Duan, “Strategy to minimize bending strain interference for flexible acoustic wave sensing platform,” *npj Flexible Electron.* **6**(1), 84 (2022).
- <sup>7</sup>J. Zhou, Y. Liu, Z. Zhan, F. Zhuo, Z. Ji, Y. Zheng, Y. Fu, and H. Duan, “Strategies for giant mass sensitivity using super-high-frequency acoustic waves,” *IEEE Sens. J.* **22**(21), 20336–20345 (2022).
- <sup>8</sup>C. Yin, J. Wu, J. Zhou, D. Zhang, Z. Liu, X. Liu, L. Liu, Z. Zhan, S. Garner, and Y. Fu, “Enhancing the sensitivity of flexible acoustic wave ultraviolet photodetector with graphene-quantum-dots decorated  $\text{ZnO}$  nanowires,” *Sens. Actuators, A* **321**, 112590 (2021).
- <sup>9</sup>Z. Ji, J. Zhou, H. Lin, J. Wu, D. Zhang, S. Garner, A. Gu, S. Dong, Y. Fu, and H. Duan, “Flexible thin-film acoustic wave devices with off-axis bending characteristics for multisensing applications,” *Microsyst. Nanoeng.* **7**(1), 97 (2021).
- <sup>10</sup>Y. Guo, J. Zhou, Z. Ji, Y. Liu, R. Cao, F. Zhuo, K. Tan, H. Duan, and Y. Fu, “A new strategy to minimize humidity influences on acoustic wave ultraviolet sensors using  $\text{ZnO}$  nanowires wrapped with hydrophobic silica nanoparticles,” *Microsyst. Nanoeng.* **8**(1), 121 (2022).
- <sup>11</sup>S. Xiong, J. Zhou, J. Wu, H. Li, W. Zhao, C. He, Y. Liu, Y. Chen, Y. Fu, and H. Duan, “Acoustic wave nitrogen dioxide sensor with ultraviolet activated 3D porous architecture of Ag-decorated reduced graphene oxide and polypyrrole aerogel,” *ACS Appl. Mater. Interfaces* **13**(35), 42094 (2021).
- <sup>12</sup>S. Liang, D. Finck, M. W. Neis, J. Schwarzkopf, D. Mayer, and R. Wördmenweber, “SAW gas sensor based on extremely thin strain-engineered  $\text{K}_{0.7}\text{Na}_{0.3}\text{NbO}_3$  films,” *Appl. Phys. Lett.* **119**(11), 112905 (2021).
- <sup>13</sup>J. Ji, Y. Pang, D. Li, Z. Huang, Z. Zhang, N. Xue, Y. Xu, and X. Mu, “An aptamer-based shear horizontal surface acoustic wave biosensor with a CVD-grown single-layered graphene film for high-sensitivity detection of a label-free endotoxin,” *Microsyst. Nanoeng.* **6**(1), 4 (2020).
- <sup>14</sup>Y. Q. Fu, J. K. Luo, N. T. Nguyen, A. J. Walton, A. J. Flewitt, X. T. Zu, Y. Li, G. McHale, A. Matthews, E. Iborra, H. Du, and W. I. Milne, “Advances in piezoelectric thin films for acoustic biosensors, acoustofluidics and lab-on-chip applications,” *Prog. Mater. Sci.* **89**, 31 (2017).
- <sup>15</sup>F. Hu, L. Cheng, S. Fan, X. Xue, Y. Liang, M. Lu, and W. Wang, “Chip-level orthometric surface acoustic wave device with AlN/metal/Si multilayer structure for sensing strain at high temperature,” *Sens. Actuators, A* **333**, 113298 (2022).
- <sup>16</sup>S. Xiong, X. Liu, J. Zhou, Y. Liu, Y. Shen, X. Yin, J. Wu, R. Tao, Y. Q. Fu, and H. Duan, “Stability studies of  $\text{ZnO}$  and  $\text{AlN}$  thin film acoustic wave devices in acid and alkali harsh environments,” *RSC Adv.* **10**(33), 19178 (2020).
- <sup>17</sup>J. Zhou, X. He, H. Jin, W. Wang, B. Feng, S. Dong, D. Wang, G. Zou, and J. K. Luo, “Crystalline structure effect on the performance of flexible  $\text{ZnO}/\text{polyimide}$  surface acoustic wave devices,” *J. Appl. Phys.* **114**(4), 044502 (2013).
- <sup>18</sup>W. Wang, P. M. Mayrhofer, X. He, M. Gillinger, Z. Ye, X. Wang, A. Bittner, U. Schmid, and J. K. Luo, “High performance  $\text{AlScN}$  thin film based surface acoustic wave devices with large electromechanical coupling coefficient,” *Appl. Phys. Lett.* **105**(13), 133502 (2014).
- <sup>19</sup>W. B. Wang, Y. Q. Fu, J. Y. Chen, W. P. Xuan, J. K. Chen, X. Z. Wang, P. Mayrhofer, P. F. Duan, A. Bittner, and U. Schmid, “ $\text{AlScN}$  thin film based surface acoustic wave devices with enhanced microfluidic performance,” *J. Micromech. Microeng.* **26**(7), 075006 (2016).
- <sup>20</sup>W. Peng, X. Jin, K. Chena, X. Li, H. Wen, B. Wanga, S. Donga, and J. Luo, “Flexible surface acoustic wave humidity sensor with on chip temperature compensation,” *Procedia Eng.* **120**, 364–367 (2015).
- <sup>21</sup>H. Xu, Z. Cao, S. Dong, J. Chen, W. Xuan, W. Cheng, S. Huang, L. Shi, S. Liu, U. Farooq, A. Qadir, and J. Luo, “Flexible dual-mode surface acoustic wave strain sensor based on crystalline  $\text{LiNbO}_3$  thin film,” *J. Micromech. Microeng.* **29**(2), 025003 (2019).
- <sup>22</sup>A. J. Smola and B. Scholkopf, “A tutorial on support vector regression,” *Stat. Comput.* **14**(3), 199–222 (2004).
- <sup>23</sup>M. A. Hearst, S. T. Dumais, E. Osuna, J. Platt, and B. Scholkopf, “Support vector machines,” *IEEE Intell. Syst. Appl.* **13**(4), 18–28 (1998).
- <sup>24</sup>L. Breiman, “Random forests,” *Mach. Learn.* **45**(1), 5 (2001).
- <sup>25</sup>G. Biau and E. Scornet, “A random forest guided tour,” *Test* **25**(2), 197–227 (2016).
- <sup>26</sup>A. Liaw and M. C. Wiener, “Classification and regression by randomForest,” *R News* **2**, 18–22 (2002).
- <sup>27</sup>Y. Lu, M. Reusch, N. Kurz, A. Ding, T. Christoph, L. Kirste, V. Lebedev, and A. Žukauskaitė, “Surface morphology and microstructure of pulsed DC magnetron sputtered piezoelectric  $\text{AlN}$  and  $\text{AlScN}$  thin films,” *Phys. Status Solidi A* **215**(9), 1700559 (2018).
- <sup>28</sup>M. Park, Z. Hao, R. Dargis, A. Clark, and A. Ansari, “Epitaxial aluminum scandium nitride super high frequency acoustic resonators,” *J. Microelectromech. Syst.* **29**(4), 490–498 (2020).
- <sup>29</sup>Y. Zhang, Y. Cai, J. Zhou, Y. Xie, Q. Xu, Y. Zou, S. Guo, H. Xu, C. Sun, and S. Liu, “Surface acoustic wave-based ultraviolet photodetectors: A review,” *Sci. Bull.* **65**(7), 587–600 (2020).
- <sup>30</sup>L. Chen, M. T. Özsü, and V. Oria, “Robust and fast similarity search for moving object trajectories,” in *Proceedings of the 2005 ACM SIGMOD International Conference on Management of Data* (Association for Computing Machinery, Baltimore, Maryland, 2005), pp. 491–502.

<sup>31</sup>D. J. Berndt and J. Clifford, "Using dynamic time warping to find patterns in time series," in *Proceedings of the 3rd International Conference on Knowledge Discovery and Data Mining* (AAAI Press, Seattle, WA, 1994), pp. 359–370.

<sup>32</sup>D. P. Huttenlocher, G. A. Klanderman, and W. J. Ruckridge, "Comparing images using the Hausdorff distance," *IEEE Trans. Pattern Anal. Mach. Intell.* **15**(9), 850–863 (1993).

<sup>33</sup>A. Botchkarev, "A new typology design of performance metrics to measure errors in machine learning regression algorithms," *Interdiscip. J. Inf. Knowl. Manage.* **14**, 045–076 (2019).

<sup>34</sup>Q. Zhang, Y. Wang, T. Wang, D. Li, J. Xie, H. Torun, and Y. Fu, "Piezoelectric smart patch operated with machine-learning algorithms for effective detection and elimination of condensation," *ACS Sens.* **6**(8), 3072–3081 (2021).

## ***Supporting Information***

### **Machine Learning Empowered Thin Film Acoustic Wave Sensing**

Kaitao Tan<sup>#,1</sup>, Zhangbing Ji<sup>#,1</sup>, Jian Zhou<sup>\*,1</sup>, Zijing Deng<sup>1</sup>, Songsong Zhang<sup>2</sup>, Yuandong Gu<sup>2</sup>, Yihao Guo<sup>1</sup>, Fengling Zhuo<sup>1</sup>, Huigao Duan<sup>1</sup>, YongQing Fu<sup>3</sup>

1 College of Mechanical and Vehicle Engineering, Hunan University, Changsha 410082, China

2 Shanghai Industrial μTechnology Research Institute (SITRI), 235 Chengbei Rd,  
201800 Shanghai, China

3 Faculty of Engineering and Environment, Northumbria University, Newcastle upon Tyne  
NE1 8ST, United Kingdom

# The same contributions

\* Corresponding E-mail: [jianzhou@hnu.edu.cn](mailto:jianzhou@hnu.edu.cn)

## **Material characterization**

Piezoelectric AlScN films with Sc concentration of ~9% were deposited on silicon using a magnetron sputtering system. The crystal orientation of AlScN film was characterized using an X-ray diffractometer (XRD-6000) with a Cu-K $\alpha$  radiation source and a scanning range of  $2\theta = 20^\circ \sim 70^\circ$ . The residual strain of the film was calculated from  $\varepsilon_z = (c - c_0)/c_0$ , where  $c_0$  is the strain-free lattice constant, and  $c$  is the lattice constant which is equal to twice the interplanar spacing  $d$ , measured from the XRD position of the (0002) peak using the Bragg equation. Surface morphology and roughness of the film were characterized using an atomic force microscope (AFM, Dimension Icon, Bruker). Cross-sectional morphology of the film was characterized using a scanning electron microscope (SEM, ZEISS Sigma300). Element composition and mapping analysis of AlScN thin films were performed using an energy dispersive spectroscopy (EDS) analyzer (Aztec X-MaxN 20 Oxford instruments). Element composition, chemical state and molecular structure of the AlScN films were analyzed using an X-ray photoelectron microscope (XPS, SHIMADZU AXIS Supra+, Japan).

## **Device parameters**

Standard UV photolithography and lift-off processes were used to fabricate two-port SAW resonators on the AlScN/Si layered structure using chromium (Cr, 10 nm)/gold (Au 50 nm) interdigital transducers (IDTs), with different wavelengths ( $\lambda$ ) of 16, 20, and 24  $\mu\text{m}$ . The SAW device had 50 pairs of IDTs with a metallization ratio of 0.5, 100 pairs of reflectors, an aperture length of 200  $\lambda$ , and the center distance between the two ports of 20  $\lambda$ .

## **UV and Temperature Test Procedure**

We selected two SAW sensitive parameters for demonstration of the principles, i.e., UV and temperature, among various multiple sensitive signals, and applied SVM and RFR algorithm to distinguish these sensitive parameters and achieve decoupling of multiple sensing parameters for thin film SAW devices. The fabricated AlScN/Si SAW devices were firstly electrically connected to the printed circuit board (PCB) using conductive silver paste with a resistance heating sheet adhered on the backside. The temperature of the SAW device was controlled by the magnitude of the output voltage through the temperature controller (OHR-

A340). A thermometer (LED, NBet Technology Co., Ltd., China) was placed near the SAW sensor, and provided the temperature readings for calibration of the dynamic temperature. For fabricating SAW UV sensing device, the ZnO nanowires (purchased from XFNANO, Nanjing, China) was coated onto the acoustic wave propagation area of the SAW device using a drop-coating process, followed by a drying process at 80 °C for 5 min to form the UV sensing layer. An UV source (LED, NBet Technology Co, Ltd, China) with a wavelength of 365 nm was used to generate UV light with different UV intensities. The device performance of the SAW devices was characterized using a vector network analyzer, and a LabVIEW-based program was developed to achieve automatic measurements and to record the frequency, phase and insert loss of SAW devices under different UV irradiation conditions and different temperatures. We conducted 16 groups of UV response experiments at 16 different temperature points (from 30 to 50 °C). For UV sensing process, a low-power UV lamp was used to irradiate the SAW device, and the irradiation hardly caused apparent changes in the surface temperatures of the SAW device. During the heating process, the temperature of the SAW device fluctuates within a range of 1°C and the temperature readings listed in the Table S1 are the average values of the temperatures on the SAW devices collected by the temperature sensor.

**Table S1. Detailed UV response experiments with 16 different temperature ranges**

Group (1-16)	Temperature (°C)	UV intensity		
<b>Group (1-4)</b>	31.7, 32.8, 33.8, 34.6	0.033mw/cm <sup>2</sup>	0.068mw/cm <sup>2</sup>	0.102mw/cm <sup>2</sup>
<b>Group (5-8)</b>	35.7, 37.1, 38.0, 39.1	0.136mw/cm <sup>2</sup>	0.170mw/cm <sup>2</sup>	0.204mw/cm <sup>2</sup>
<b>Group (9-12)</b>	40.6, 41.8, 42.7, 44.6	0.237mw/cm <sup>2</sup>	0.270mw/cm <sup>2</sup>	0.305mw/cm <sup>2</sup>
<b>Group (13-16)</b>	45.2, 45.7, 46.6, 48.5	0.337mw/cm <sup>2</sup>	0.369mw/cm <sup>2</sup>	0.403 mw/cm <sup>2</sup>

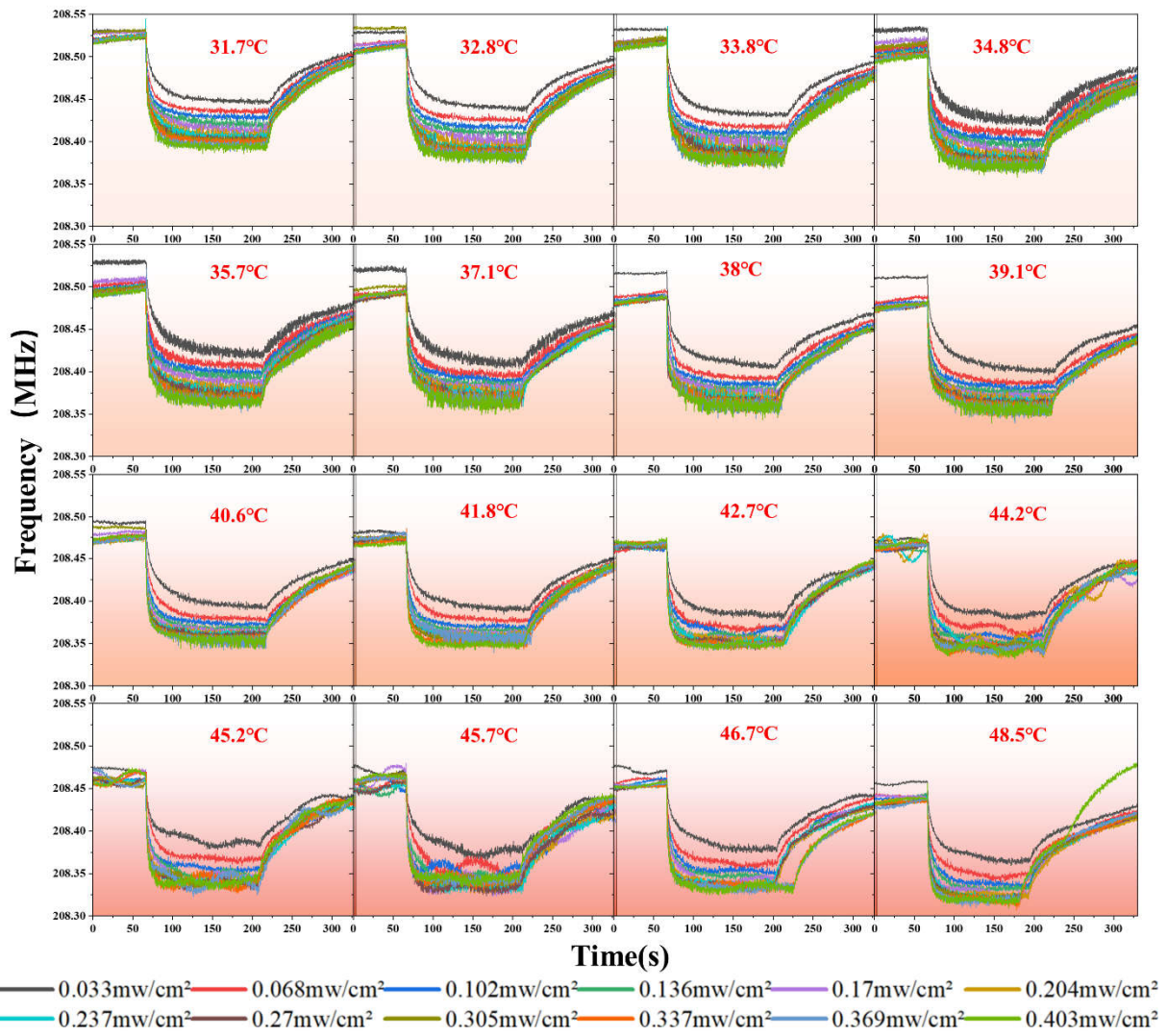


**Figure S1** The changes of resonant frequencies of the SAW device under different UV intensities (0.033 ~0.403 mw/cm<sup>2</sup>) at various temperatures (31.7 ~ 48.5 °C).

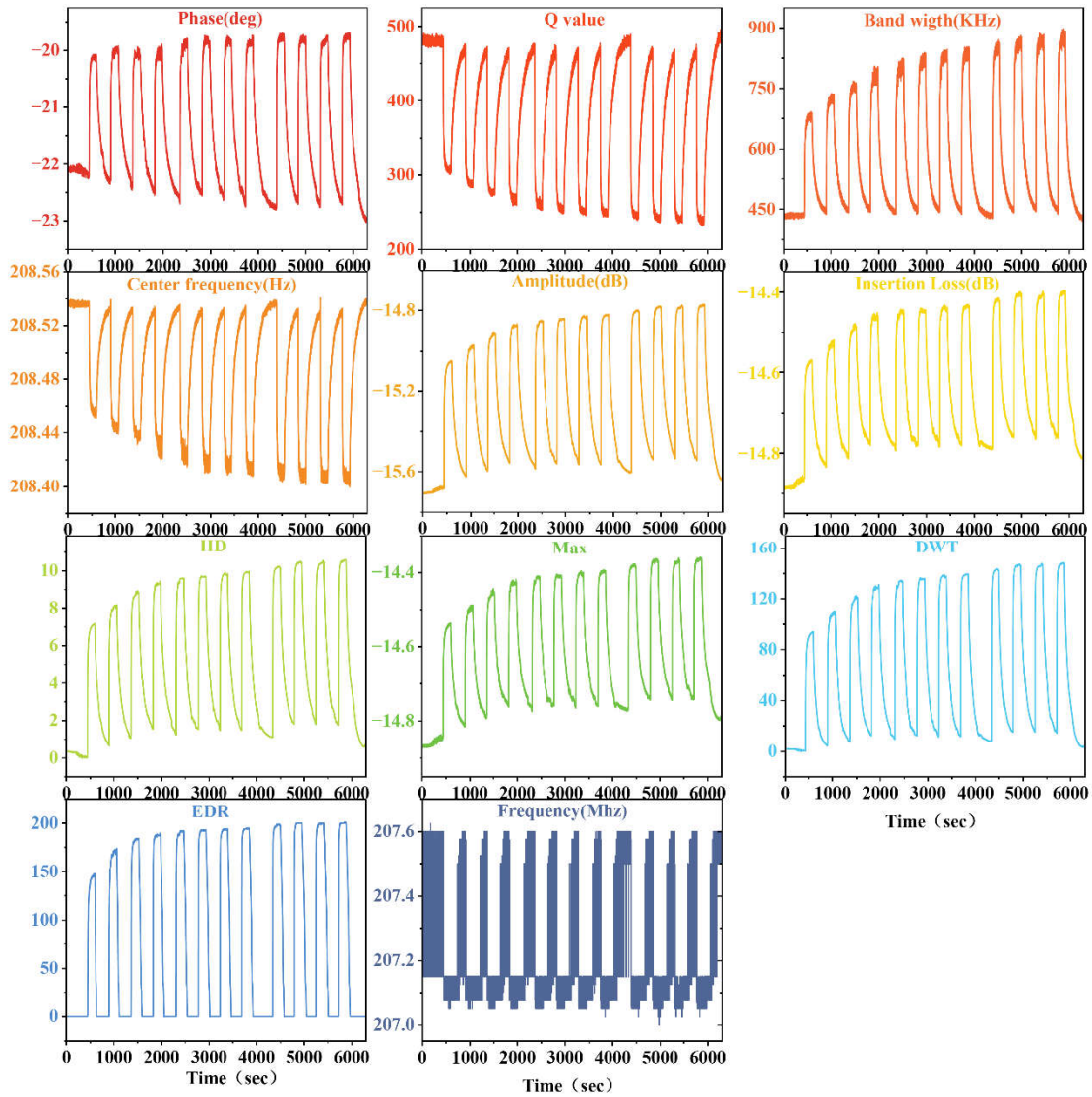


**Figure S2** Eleven features (Phase, Q value, Band width, Center frequency, Amplitude, Insertion Loss, Hausdorff distance, Maximum value, Dynamic time warping, Edit distance on real sequence, Frequency) extracted from scattering parameter ( $S_{21}$ ) responses of the SAW device ( $\lambda$  of 24  $\mu\text{m}$ ) changes with the changes of UV intensities from 0.033mw/cm<sup>2</sup> to 0.403 mw/cm<sup>2</sup>, under a temperature of 31.7°C.

### The Calculation Methods for 11 Features of SAW

The transmission ( $S_{21}$ ) and reflection ( $S_{11}$ ) spectra of the SAW devices were obtained using a vector network analyzer and a LabVIEW program. We directly obtained seven features including Frequency, Amplitude, Band width, Center frequency, Insertion Loss, Phase, Q value from the transmission ( $S_{21}$ ) and reflection ( $S_{11}$ ) spectra of the SAW devices [1, 2]. From the physical mechanisms of SAW propagation, these features are mainly the combinations of one or more information such as the velocity of sound in the medium, impedance/loss, the propagation time of sound waves in the sensitive area. For example, the resonant frequency

mainly contains the equivalent sound velocity of the medium. The phase characteristics information contains combination of sound velocity of the medium and propagation time of sound waves in the sensitive region. The quality factor contains the device impedance information. The other four features of Hausdorff distance, Edit distance on real sequence, Maximum value and Dynamic time warping were calculated by using the following introduced methods. We calculated these four features one by one using the MATLAB program.  $S_0$  is the amplitudes of the  $S_{21}$  parameters in the selected frequency band (i.e.,  $S_{21}$  vector) under initial UV intensity and temperature.  $S$  is the amplitudes of the  $S_{21}$  parameters in the selected frequency band (i.e.,  $S_{21}$  vector) under the next/later UV intensity and temperature. Here are the details of the four functions for these features.[3]

### ***Hausdorff distance(HD)***

According to Ref.[4], the Hausdorff distance can be defined as

$$H(S, S_0) = \max(h(S, S_0), h(S_0, S))$$

Where

$$h(S, S_0) = \min_{a \in S} \max_{b \in S_0} |a - b|$$

### ***Edit distance on real sequence (EDR)***

According to Ref. [5], the EDR is defined as the number of operations (insert, delete, or replace) that are needed to change  $S$  into  $S_0$ , which takes the form

$$\begin{aligned} EDR(S, S_0) = \min & \{EDR(Rest(S), Rest(S_0)) + subcost, \\ & EDR(S, Rest(S_0)) + 1\} \\ & subc \begin{cases} 0, & \text{if } |S(1) - S_0(1)| \leq tol \\ 1, & \text{otherwise} \end{cases} \end{aligned}$$

where the function Rest( $S$ ) is defined as the sub-matrix of  $S$  without the first element and the  $tol$  denotes the tolerance of matching (matching threshold). In this paper, the  $tol = 0.4$  according to practical needs.

### ***Maximum value(Max)***

The maximum value is calculated by searching the maximum values of the amplitudes of the  $S_{21}$  parameters in the selected frequency band (i.e.,  $S_{21}$  vector) under a certain UV intensity and temperature .

### ***Dynamic time warping (DTW)***

The value of the fourth feature is defined as the distance between  $S$  and  $S_0$  using the dynamic time warping (DTW) technique. We assume that  $S = [a_1, a_2, \dots, a_i, \dots, a_n]$ ,  $S_0 = [b_1, b_2, \dots, b_j, \dots, b_n]$ . According to Ref.[6], the two sequences can be arranged to form a n-by-n grid, and a path can be generated starting from the point  $(a_1, b_1)$  and ending at the point  $(a_n, b_n)$ . The warping path  $W = [w_1, w_2, \dots, w_k, \dots, w_m]$  and each  $w_k$  corresponds to a point  $(i, j)_k$ . To form the warping path, several restrictions are adopted, including

$$(i, j)_1 = (1, 1), (i, j)_k = (n, n)$$

$$(i, j)_k = (i - 1, j)_{k-1} \text{ or } (i, j - 1)_{k-1} \text{ or } (i - 1, j - 1)_{k-1}$$

With the distance defined as  $\delta(i, j) = (a_i - b_j)^2$ , the DTW distance can be obtained by

$$DTW(S, S_0) = \min \left[ \sum_{k=1}^m \delta(w_k) \right]$$

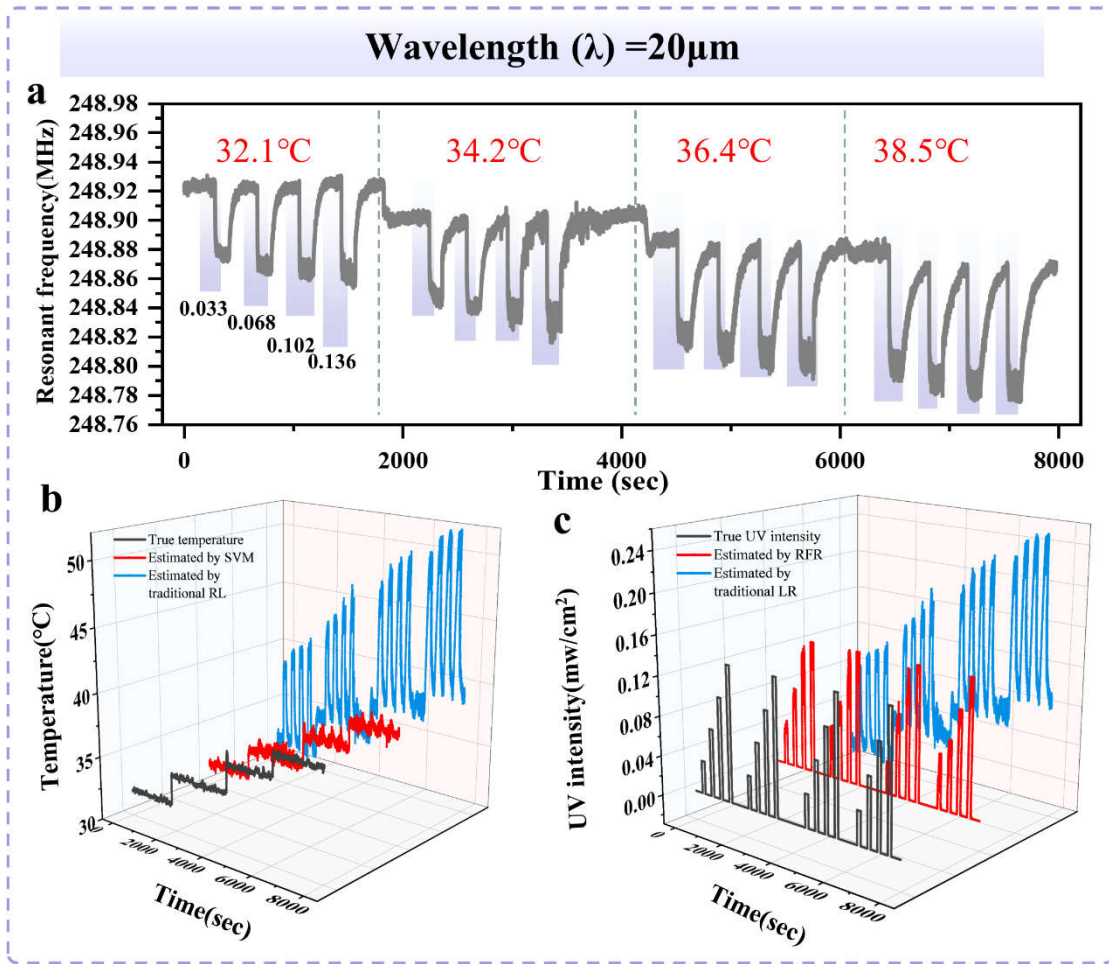


**Figure S3** (a) Resonant frequencies of SAW devices with  $\lambda$  of 20  $\mu\text{m}$  under different UV light intensity and temperature; (b) Comparison of the temperature predicted results by the traditional linear regression model and proposed SVM model for the SAW device with  $\lambda$  20  $\mu\text{m}$ ; (c) Comparison of the predicted UV results by the traditional linear regression model and the proposed RFR model for the SAW device with  $\lambda$  of 20  $\mu\text{m}$ .

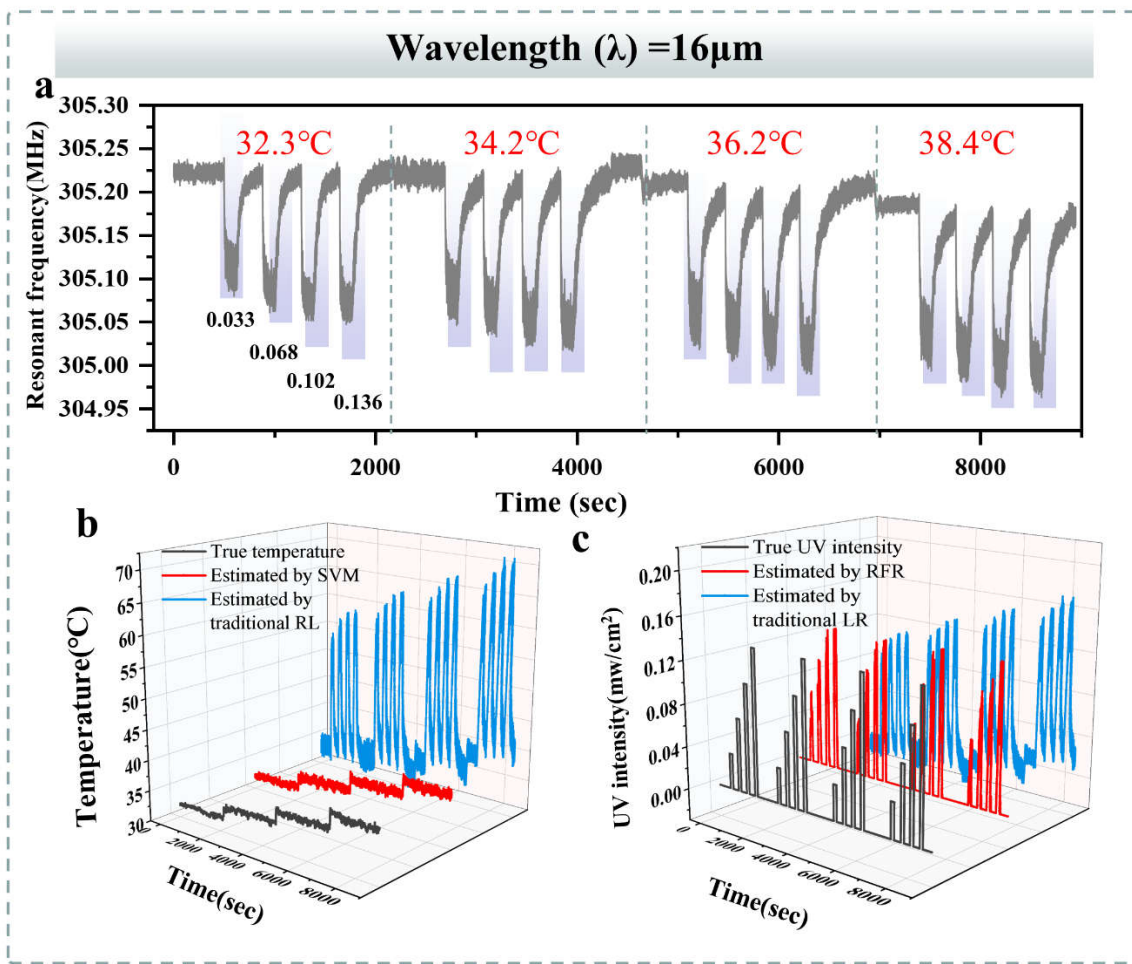


**Figure S4** (a) Resonant frequencies of SAW devices with  $\lambda$  of 16  $\mu\text{m}$  under different UV light intensity and temperature; (b) Comparison of the temperature predicted results by the traditional linear regression model and proposed SVM model for the SAW device with  $\lambda$  16  $\mu\text{m}$ ; (c) Comparison of the predicted UV results by the traditional linear regression model and the proposed RFR model for the SAW device with  $\lambda$  of 16  $\mu\text{m}$ .

## Reference

1. Wu, J.H., et al., Ultrathin Glass-Based Flexible, Transparent, and Ultrasensitive Surface Acoustic Wave Humidity Sensor with ZnO Nanowires and Graphene Quantum Dots. *Accts Applied Materials & Interfaces*, **12**(35) 39817-39825 2020.
2. He, X.L., et al., High performance dual-wave mode flexible surface acoustic wave resonators for UV light sensing. *Journal of Micromechanics and Microengineering*, **24**(5) 2014.
3. Zhang, Q., et al., Piezoelectric Smart Patch Operated with Machine-Learning Algorithms for Effective Detection and Elimination of Condensation. *ACS Sens*, **6**(8) 3072-3081 2021.
4. Huttenlocher, D.P., G.A. Klanderman, and W.J. Rucklidge, Comparing images using the Hausdorff distance. *IEEE Transactions on Pattern Analysis and Machine Intelligence*, **15**(9) 850-863 1993.
5. Chen, L., M.T. Özsü, and V. Oria, Robust and fast similarity search for moving object

- trajectories, in Proceedings of the 2005 ACM SIGMOD international conference on Management of data. 2005, Association for Computing Machinery: Baltimore, Maryland. 491–502 2005.
6. Berndt, D.J. and J. Clifford, Using dynamic time warping to find patterns in time series, in Proceedings of the 3rd International Conference on Knowledge Discovery and Data Mining. 1994, AAAI Press: Seattle, WA. 359–370 1994.